EXPERIMENTAL OPTIMIZATION OF MECHANICAL PERFORMANCE IN T6 HEAT-TREATED ALUMINUM ALLOY A380 WITH MACHINE LEARNING-BASED PREDICTION OF SPECIFIC WEAR BEHAVIOR

Ahmet Tigli
Department of Metallurgical and Materials Engineering, Sinop University, 57000 Sinop, Turkey

Huseyin Kose and Ismail Bayar
Department of Mechanical Engineering, Batman University, 72001 Batman, Turkey

https://doi.org/10.1007/s40962-025-01801-6

Abstract

This study investigates the influence of quenching temperature, aging temperature, and time on the mechanical properties of gravity die-cast A380 aluminum alloys subjected to T6 heat treatment. Samples were aged at 175°C and 275°C for different time periods, with quenching performed at 20°C and 80°C. The effects of heat treatment on microstructure, tensile strength, wear behavior, and hardness were evaluated. The results demonstrated that ultimate tensile strength increased substantially from 165 MPa to 275 MPa at an aging temperature of 175°C, whereas a higher aging temperature of 275°C did not provide any additional improvement. In contrast, hardness showed a strong dependence on aging duration at 175°C, rising from 108 HV to 152 HV. However, at 275°C, hardness declined significantly, reaching as low as 80 HV. The highest wear resistance was achieved in the samples quenched at 20°C and aged at 275°C for 6 hours, exhibiting an 81.2% improvement compared to the untreated sample. These findings provide valuable insights for optimizing the heat treatment process of A380 aluminum alloys in industrial applications, particularly in improving mechanical properties for automotive and aerospace components. The specific wear rate was estimated using various machine learning algorithms within the framework of data-driven approaches using the obtained experimental data. Model performances were compared in training, test, and validation sets; Random Forest and Deep Neural Network models stood out with their high accuracy and generalization abilities. While the Random Forest model showed low error rate and high stability, the Deep Neural Network model attracted attention with the lowest MSE (≈ 1.7) and highest R^2 score (≈ 0.85), especially in the test set.

Keywords: *aluminum, A380, heat treatment, tensile, hardness, wear, machine learning*

Introduction

The demand for lightweight metals is increasing due to the high strength-to-weight ratio which offers significant advantages in applications where lightweight materials are preferred. Among these metals, aluminum alloys are widely preferred in various industrial sectors such as aerospace and automotive where both performance and weight reduction are critical design considerations.[1,2] One of the most commonly utilized aluminum alloys in the applications is aluminum A380. This alloy is specifically preferred for engine blocks, and cylinder heads due to low density, good castability, mechanical properties, corrosion, and wear resistance.[3,4]

Aluminum A380 alloys can be produced by various casting methods that have been extensively investigated in the literature.[5] Gencalp and Saklakoglu[6] investigated the vibration effect on the A380 alloy casting by cooling slope. Seifeddine and Svensson[7] studied A380 die-casting with various Mg and Fe content to understand the solidification rate effect on the microstructure and mechanical properties. Obiekea, et al.[8] investigated the pressure effect on die-cast

Received: 05 June 2025 / Accepted: 31 October 2025
Published online: 12 November 2025

A380 alloy. The mechanical properties of A380 aluminum alloy can be significantly improved through the selection of an appropriate casting method. In particular, advancements in casting techniques such as effective degassing processes and the use of grain refiners have been shown to enhance the alloy's structural integrity and performance characteristics.[5] Gecu, et al.[9] investigated T6 heat treatment (HT) effect on A380 alloys manufactured through a combination of thixoforging and low superheat casting techniques. The cast A380 samples were maintained at semi-solid regions at 575°C, and from 20 to 80 minutes. Following this, a 4-hour solution treatment of the A380 process is conducted at 520°C, quenched in water, and aged at 180°C for 4 hours. In most cases, high, medium, and low hardness values are observed in the artificially aged, thixoforged, and solution-treated samples, respectively. The T6 HT resulted in precipitation of Al_2Cu in the α(Al) matrix of the A380 alloy, which is responsible for the increase in hardness.

In addition to selecting the casting techniques, mechanical properties can also be altered by using different HT methods, where different parameters can be selected and optimized to enhance the performance. Among various HT techniques, the T6 HT is one of the most commonly applied methods for A380 alloys due to its ability to substantially improve strength and hardness.[10] T6 HT consists of three stages: (i) solution treatment, (ii) quenching following the solution treatment, and (iii) aging.

Research on the effects of HT on aluminum alloys' mechanical properties has been ongoing for decades in the literature. Khisheh, et al.[11] investigated the HT effect on the high-cycle fatigue properties of A380. The T6 HT parameters are at 510°C for 5 hours, air-cooled, and aged at 200°C for 3 hours. The T6 HT improved the fatigue lifetime of the material, ranging from 26% to 85% across various stress levels. Yuan, et al.[12] investigated aging treatment on the microstructure of a high-pressure die-cast A380 alloy. The specimens were heated to 490°C for 30 minutes and quenched in water. Some of these specimens were immediately aged for different periods (ranging from 0 to 120 hours) at 150°C. The hardness values significantly changed at the surface (exhibit higher hardness values) and center regions of the T6 HT samples. The max hardness is observed after 20-25 hours of aging at 150°C. On the other hand, the hardness values decline with increasing aging time beyond 60 hours of aging. In another study, Yang, et al.[13] investigated the effects of T6 HT on A380 alloys. The solution treatment is conducted at 510°C for 30 minutes and quenched in cold water. Aging treatment is performed at 170°C for 4 hours. They state that the hardness of the A380 alloy, containing 0.3 wt.% Mg, increased from 100 to 160 HV with an increasing aging time. Additionally, they reported that the T6 HT A380 alloy exhibited 282 MPa yield strength and a 4.2 % elongation.

In this study, the effects of T6 HT parameters—including quenching temperature, aging temperature, and aging time—on mechanical properties of A380 aluminum alloy produced by gravity die-casting technique were systematically investigated. Critical performance criteria such as tensile strength, micro hardness, and specific wear rate were evaluated with comprehensive experimental studies. Thereby, optimum HT conditions were determined. In addition to comprehensive experimental analysis, data-driven prediction models are developed with decision trees, ensemble algorithms, and artificial neural network-based regression models with the obtained specific wear rate data. In this way, both practical suggestions for optimizing mechanical properties are presented and advanced predictive models for the wear behavior of A380 alloy are created, thus making a multifaceted contribution to literature.

Methodology

Casting Process

In this study, prior to the casting process, the permanent mold was coated with an Al_2O_3 solution to enhance the fluidity and filling rate of the mold. Additionally, the coated mold was preheated to a temperature range of 250 to 300°C to prevent any potential defects in the resulting cast cylindrical bars. The chemical composition (wt.%) of A380 alloy is presented in Table 1.

A380 ingots were melted in a 300-kg SiC crucible using an industrial resistance furnace at 750°C. The degassing process was not applied to the molten A380. The gravity die-casting process was performed in a permanent mold with 6 cylindrical test bars. Upon completion of the casting process, the cylindrical bars were separated from the basin and runners.

Heat Treatment

The heat treatment (HT) protocol involved a solution treatment stage conducted for 3 hours at a temperature of 520°C in a resistance furnace. The samples were

Table 1. Composition of the A380 Aluminum Alloys

Alloy	Si	Fe	Cu	Mn	Mg	Zn	Ti	Ni	Al
A380	8.706	0.232	3.570	0.109	0.081	0.013	0.035	0.007	rem

maintained at an annealing temperature for 1 hour to facilitate stress relief and promote uniform grain structure. After annealing, samples were exposed to quenching in both cold water (20°C) and hot water (80°C). Upon completing the quenching process, the samples were subjected to aging at temperatures of 175°C and 275°C for three distinct durations: 6 hours, 12 hours, and 18 hours. The samples were then cooled in ambient conditions. The temperatures used in this research were chosen based on preliminary studies and literature review, considering the alloy's phase transformation behavior. The time durations for HT at each temperature were specifically selected to study the impact of prolonged exposure on mechanical properties. All procedures including solution treatment, quenching, and artificial aging are shown in Figure 1. The HT parameters with sample names are given in Table 2

Microstructure

In order to evaluate the effects of T6 HT on the microstructure of A380 aluminum alloy, metallographic sample preparation methods were applied. Afterward, samples required for microstructure examinations were taken from the middle regions of the castings. The prepared samples were grinded with silicon carbide (SiC) grinding disks and then polished with Metkon Forcipol 202 device using 3 µm and 1 µm diamond suspensions. Following the polishing process, the samples were etched with Keller reagent (3A) for 15–20 seconds to reveal microstructural details. This reagent consists of 1mL HF, 1.5mL HCl, 2.5mL HNO_3, and 95mL distilled water. Optical microstructure observations were performed with a Nikon Eclipse MA100N optical microscope. Detailed analyses of surface morphology and phase distribution were performed with a Thermo Scientific Apreo 2S model scanning electron microscope (SEM).

Mechanical Tests

Mechanical properties were evaluated using universal testing machines, measuring parameters such as tensile strength, hardness, and wear resistance.

After the die-casting process, the samples were machined into standardized samples according to ASTM E8/E8M for the tensile test to ensure consistency in the experimental setup. The dimensions of samples used in the tensile tests are shown in Figure 2. The samples prepared for the tensile test were subjected to uniaxial loading with computer-controlled Shimadzu AG-IC testing machine to evaluate the ultimate tensile strength, and elongation at fracture. At least three tensile tests were carried out for each test parameter at room

Table 2. Design of Experiment

Sample	Quenching temperature (°C)	Aging temperature (°C)	Aging duration (h)
NT	No treatment		
Q2A1T6	20	175	6
Q2A1T12	20	175	12
Q2A1T18	20	175	18
Q2A2T6	20	275	6
Q2A2T12	20	275	12
Q2A2T18	20	275	18
Q8A1T6	80	175	6
Q8A1T12	80	175	12
Q8A1T18	80	175	18
Q8A2T6	80	275	6
Q8A2T12	80	275	12
Q8A2T18	80	275	18

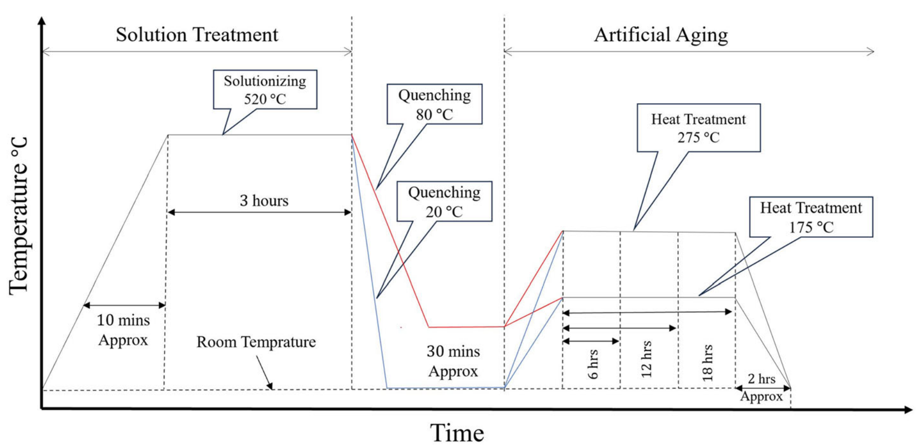

Figure 1. Schematic illustration of T6 HT procedures.

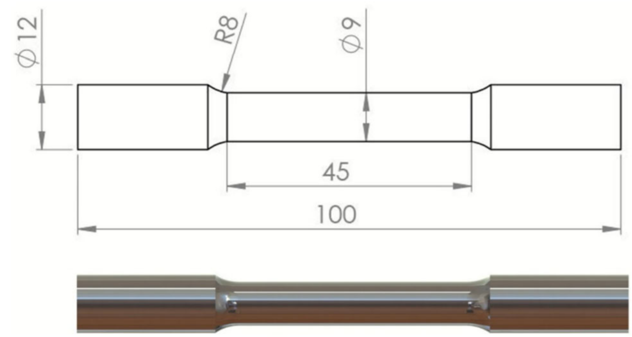

Figure 2. Dimension of the test samples.

temperature, 50% humidity and a constant speed of 2 mm/min. SEM images of the fractured surfaces were investigated to determine the fracture modes of the tensile samples.

Micro-Vickers hardness tests were conducted to assess the material's resistance to plastic deformation. The samples were cut into $\phi 12mm x 5mm$ dimensions for the hardness test. The AFRI DM8 hardness tester machine was used for micro-Vickers hardness tests (HV) with 1 kgf load with 10 seconds dwell time for A380 aluminum alloy samples. Hardness values for each sample were determined by calculating the average measurement taken from 5 points. The hardness values were calculated using Eqn. 1.

$$HV = 1.854 \frac{F}{D^2} \qquad \text{Eqn. 1}$$

where F and D are the applied force (kilogram-force) and indent diagonals (mm), respectively.

The wear tests were carried out with ball-on-disk geometry according to the ASTM G99 test standard. Certified AISI 304 stainless steel balls with a diameter of 6 mm were used as the counter body. Samples were prepared by using the wet abrasive cutting method in the dimensions of Ø12 mm x10 mm. Wear samples were cut from the central region of the HT samples. Following the cutting process, the surface of all samples was ground and polished to a surface roughness (Ra) of 0.2 μm. Tests were carried out under room conditions. Other parameters are as follows: load 5 N, wear scar diameter 6mm, distance 60 m, and speed 3 cm/s. After the tests, the samples' wear rates and coefficients of friction (COF) were determined and compared. The wear rates were calculated by measuring the wear scarfs. Additionally, SEM/ EDS analysis of a selected sample was also evaluated.

Machine Learning and Neural Network-Based Modeling Approach

In this study, machine learning (ML) and artificial neural network (ANN)-based regression approaches were used to model the effects of different HT conditions applied to A380 aluminum alloy on the specific wear rate. A dataset consisting of 52 experimentally obtained measurements used to train the regression models. The dataset contains three inputs and one output: the input variables are quenching temperature, aging temperature, and aging time, and the output variable is the specific wear rate. The input parameters were carefully chosen because they represent the fundamental heat treatment variables that directly control precipitation kinetics, microstructural evolution, and consequently wear behavior in aluminum alloys. Restricting the feature space to these experimentally controlled parameters ensures both physical interpretability and a direct causal relationship between process conditions and material response. The dataset used in this study consists of a controlled and optimized number of measurements required by experimental design. Studies that reliably examine wear behavior through a limited number of experiments with high information content are widely studied in the tribology and materials engineering literature.[14,15]

Prior to analysis, possible categorical variables were encoded into numerical form using a label encoder, and all input variables were normalized to zero mean and unit variance using the standard scaler to eliminate scale differences. Following preprocessing, the dataset was divided into training (70%), testing (20%), and validation (10%) subsets to ensure a balanced evaluation of learning and generalization performance.

Classical ML models (DT, RF, GB, XGB), the ANN-based MLPR, and a Deep Neural Network (DNN) were implemented. ML models were implemented with their default hyperparameters. MLPR was structured with a two-hidden layer architecture (128 neurons per layer), with a ReLU activation function and the Adam optimization algorithm used in each layer, and a maximum iteration number of 300. DNN model was designed with four hidden layers consisting of 128, 64, 32, and 16 neurons, respectively; ReLU activation was used in all hidden layers and a linear activation function was used in the output layer, and the model was trained for a maximum of 150 epochs with a batch size of 16. The model was trained with the Adam optimization algorithm, with a mean squared error loss function set as the optimization target. The schematic view of ANN-based models is shown in Figure 3.

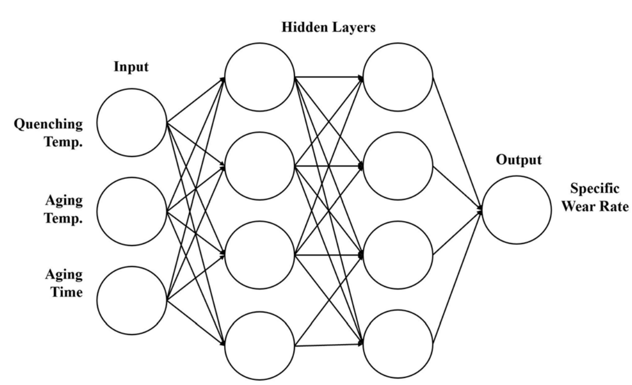

Figure 3. Schematic view of ANN-based models.

Model performance evaluation was carried out using a k-fold cross-validation procedure, with the number of folds set to five, in order to enhance the robustness of generalization assessment and to further mitigate the risk of overfitting. Furthermore, model complexity was limited appropriately to the dataset size to reduce the risk of overfitting. Early stopping was applied to ANN-based models, and hyperparameter bounds were used to prevent excessive branching in decision tree-based models. Absolute percentage error (APE) and mean absolute percentage error (MAPE) were calculated using Eqns. 2 and 3 as a metric for performance monitoring. Furthermore, model performance was evaluated not only on the training set but also on validation sets using MSE and R^2 metrics calculated with Eqns. 4 and 5, respectively. This ensures the generalization capabilities of the models.

$$\mathrm{APE} = \left|\frac{y_i - \hat{y}_i}{y_i}\right| \times 100\% \qquad \text{Eqn. 2}$$

$$\mathrm{MAPE} = \frac{100\%}{n}\sum_{i=1}^{n}\left|\frac{y_i - \hat{y}_i}{y_i}\right| \qquad \text{Eqn. 3}$$

$$\mathrm{MSE} = \frac{1}{n}\sum_{i=1}^{n}(y_i - \hat{y}_i)^2 \qquad \text{Eqn. 4}$$

$$\mathrm{R}^2 = 1 - \frac{\sum_{i=1}^{n}(y_i - \hat{y}_i)^2}{\sum_{i=1}^{n}(y_i - \bar{y})^2} \qquad \text{Eqn. 5}$$

Here, y_i and $\hat{y}_i$ denote the actual and predicted value, respectively, $\bar{y}$ represents the mean of actual values and n denotes the total number of observations.

Results and Discussion

Microstructure

Figure 4 presents the microstructures of the A380 alloy were subjected to various heat treatment (HT) conditions. In the as-cast state without any post-casting HT (Figure 4a), the microstructure remains in its original form. The microstructure of A380 alloy primarily consists of primary aluminum, eutectic silicon, and β-phase platelets. In the as-cast condition without HT (Figure 4a), the microstructure exhibits a typical dendritic structure for the primary aluminum phase, along with needle-like eutectic silicon and the presence of β-phase platelets. Figure 4b shows the microstructure of the A380 alloy after quenching in 80 °C water followed by aging at 175 °C for 6 hours. While the dendritic structure of the primary aluminum phase is largely retained, partial spheroidization of the eutectic silicon phase is observed, with some of the needle-like structures transforming into more rounded, spheroidal forms. This microstructural evolution may contribute to the observed improvement in tensile strength, increasing from 165 MPa in the as-cast condition to 265 MPa after aging at 175 °C for 6 hours following 80 °C quenching. Figure 4c presents the microstructure of the A380 alloy after quenching in 80 °C water followed by aging at 275 °C for 6 hours. In this condition, the eutectic silicon phase undergoes significant morphological transformation, with the previously needle-like structures becoming coarsely spheroidized. This coarsening of the silicon particles may be a contributing factor to the reduction in tensile strength, which decreases from 265 MPa (observed in the 80 °C quenched and 175 °C

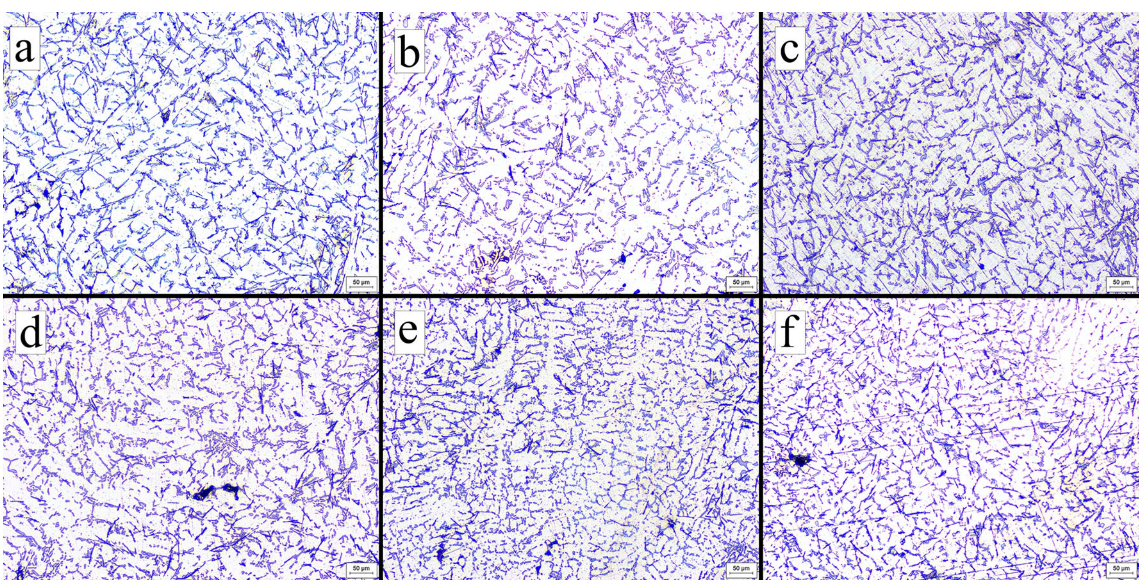

Figure 4. Microstructures of A380 alloy under different HT conditions: (a) NT, (b) Q8A1T6, (c) Q8A2T6, (d) Q2A1T6, (e) Q2A1T12, (f) Q2A1T18.

aged for 6 hours condition) to 165.2 MPa. Figure 4d to f illustrate the microstructures of the A380 alloy aged for 6, 12, and 18 hours at 175 °C after quenching in 20 °C water. In all three conditions, spheroidization of the eutectic silicon phase is clearly observed. As the aging time increases, the spheroidized silicon particles become progressively coarser, indicating continued coarsening of the eutectic phase with prolonged thermal exposure.

The microstructural images reveal that the A380 aluminum alloy retains its dendritic structure both before and after HT, with no significant change in the overall microstructure size. However, HT induces a clear transformation of the eutectic silicon phase, changing its morphology from needle-like to a more spheroidized form across all treated conditions. Sjölander and Seifeddine[16] state that spheroidization of eutectic Si particles has a significant impact on the mechanical properties of aluminum alloys. In their needle-like morphology (large brittle flakes in unmodified alloys), Si particles act as crack initiators and reduce ductility. Ogris et al.[17] stated that the spheroidization of eutectic silicon during T6 heat treatment of Al-Si alloys is responsible for the improved ductility of these alloys. Wang et al.[18] investigated the effect of eutectic Si spheroidization on the elongation and tensile strength of eutectic Al-Si alloys by annealing at 500 and 560°C for 1, 2, 3, 4, 5, 7, and 10 h. They reported that the flake-like Si phase gradually transformed into rod-like or granular morphologies. As a result, the tensile strength decreased from 194 MPa to 171 MPa, while the elongation increased from 6.3% to 10.5%.

SDAS is one of the key parameters that affect the mechanical properties of aluminum alloys. Borkar et al.[19] reported that increasing SDAS from 9 to 27 μm resulted in a decrease in ultimate tensile strength (UTS) from 272 to 225 MPa, while the elongation decreased from 3 $\pm$ 0.7% to 2.22 $\pm$ 0.4%. Similarly, Ceschini et al.[20] studied the heat treatment of A354 alloys with different SDAS values. They found that samples with finer SDAS (20 $\pm$ 2 μm) exhibited higher UTS (346 $\pm$ 3 MPa) and elongation (5.9 $\pm$ 0.8%) compared to samples with coarser SDAS (44 $\pm$ 3 μm), which showed lower UTS (294 $\pm$ 5 MPa) and elongation (1.1 $\pm$ 0.4%). In this study, the measured SDAS and secondary dendrite arm length (SDAL) values are approximately 20 μm and 120 μm, respectively, for both non-HT and HT samples. Therefore, although changes in SDAS and SDAL can influence mechanical properties, in this work these parameters remained essentially constant, and the observed changes in mechanical properties after heat treatment cannot be attributed to them. Figure 5 presents the microstructure observed at 500× magnification.

Figure 5a, b, and c correspond to samples quenched at 20°C and 80°C, followed by aging at 175°C for durations of 6 and 18 hours. Figure 5d depicts a sample quenched at 80°C and subsequently aged at 275°C for 6 hours. In the images, the phases identified include α-Al, α-Fe (characterized by a Chinese script morphology), β-Fe (needle-like structure), and the Si phase, which are indicated by red arrows. The presence of α-Al, Si, α-Fe, and β-Fe phases in the microstructure is consistent with previous studies on A380 alloy.[21,22]

Figure 6 presents the EDS analysis of samples aged at 275 °C for 6 hours and quenched at 20°C. The oxygen distribution appears uniform, with no evidence of localized concentration, indicating the absence of oxide inclusions in the microstructure. Similarly, Cu is evenly distributed, showing no signs of segregation. The main purpose of T6 heat treatment is to homogenize segregated Cu during solution treatment and to promote the formation of fine Cu precipitates during aging. Therefore, the T6 heat treatment applied to the A380 alloy can be considered successful. In addition, Mg also exhibits a uniform distribution without segregation. This even distribution of Cu and Mg suggests that the $CuAl_2$ and Mg_2Si phases are finely dispersed throughout the structure without significant clustering.

Figure 7a and b present SEM images of Q2A1T6 sample. In Figure 7a, the distribution of silicon (Si) and iron (Fe) phases is clearly observed, while Figure 7b distinctly shows a Chinese script-shaped α-iron (α-Fe) intermetallic phase approximately 50 μm in size.

Similarly, Figure 7c and d depict Chinese script-shaped intermetallic phases measuring approximately 50–60 μm, along with a silicon phase of about 40 μm that is homogeneously distributed within the aluminum matrix. Figure 7e and f display SEM images of samples quenched in water at 80 °C and aged at 175 °C for 18 hours. In these images, pine tree-like structures corresponding to the α-iron intermetallic phase are clearly visible.

Tensile Test

The tensile strength for the untreated A380 aluminum alloy specimen was 165.3 MPa. This value is as a reference point for assessing the impact of different HT processes on the alloys' mechanical strength. The tensile test results showed in Figure 8 revealed a complex correlation between the HT conditions, quenching temperatures, and time durations. Most specimens except several have shown significant improvement in tensile strength after HT, demonstrating the importance of controlled HT processes in optimizing the mechanical properties of aluminum alloy A380 for a variety of applications.

The experimental data indicates that the duration of HT has a profound influence on the tensile properties of the A380 aluminum alloy. As observed, the tensile strength decreases with increasing HT duration. Specifically, Q2A1T6 sample exhibited the highest tensile strength of 274.7 MPa,

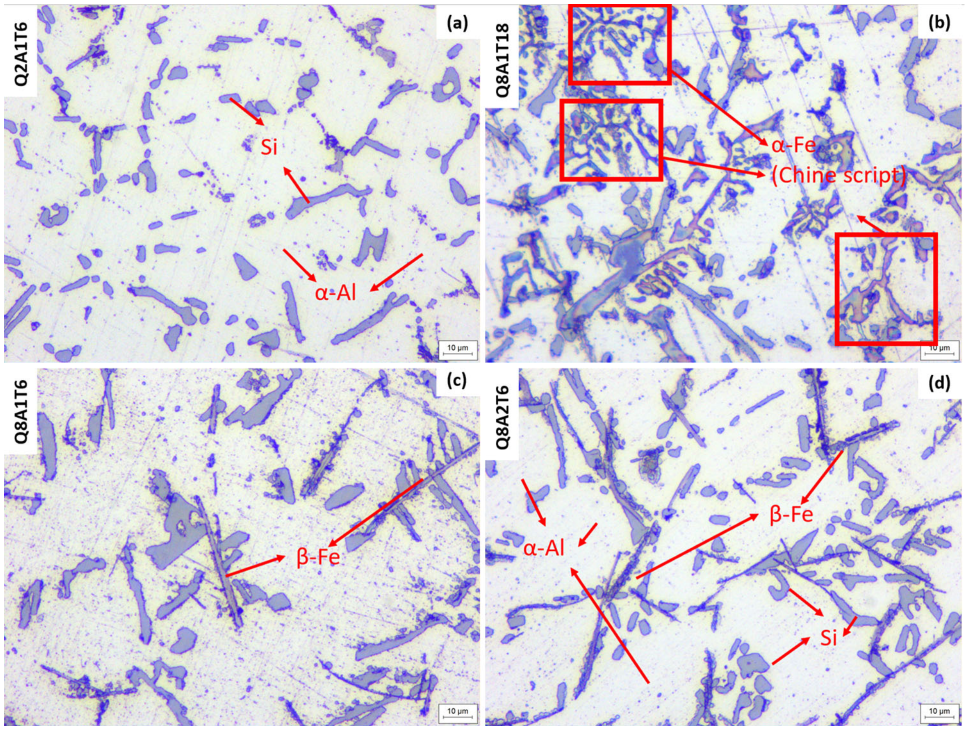

Figure 5. An observation of the microstructure at 500× magnification.

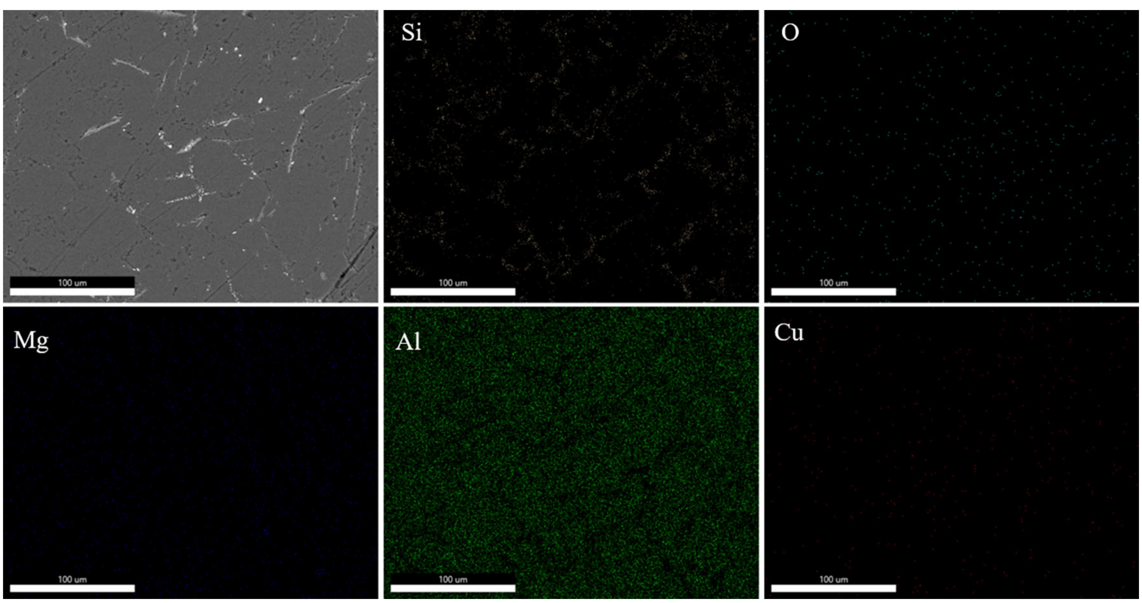

Figure 6. EDS mapping of Q2A2T6 sample.

which gradually decreased to 266.9 MPa for sample treated for 12 hours, and further dropped to 218.5 MPa for sample exposed to 18 hours of HT. The changes in tensile strength during HT at 175°C can be attributed to the precipitation and aging of strengthening phases in the material. Initially, as precipitates form during HT, tensile strength increases due to the enhanced pinning of dislocations. However, beyond a certain point, excessive aging led to coarsening of these precipitates, which has weakened the material. This suggests that there is an optimal duration for HT at 175°C, beyond which over-aging occurs, resulting in reduced tensile strength. During over-aging, the precipitates within the alloy can grow excessively in size.[23] These larger precipitates are less effective at hindering dislocation movement, leading to a reduction in tensile strength. The formation and growth of coarse intermetallic phases, such as Mg_2Si, during prolonged exposure to elevated temperatures tend to weaken the overall material structure, leading to the observed reduction in tensile strength.[24]

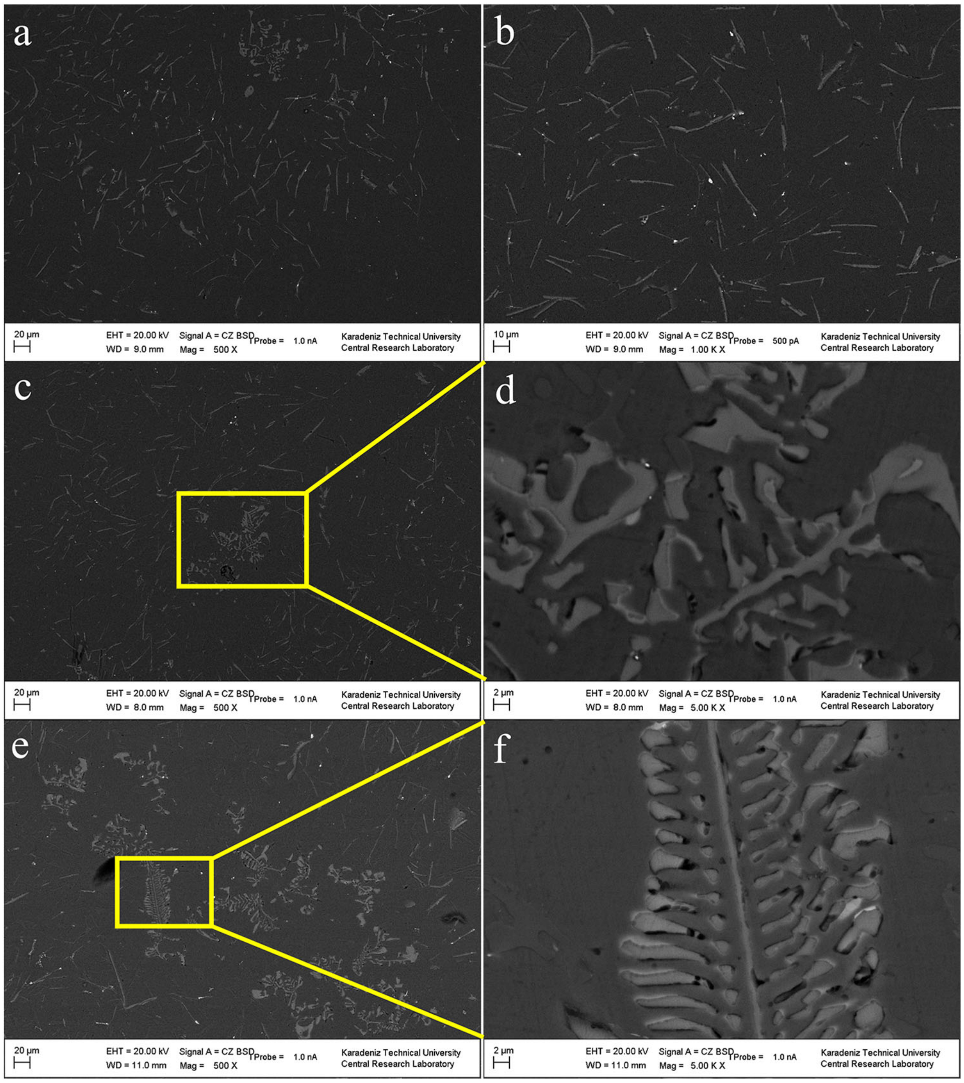

Figure 7. SEM images of samples (a)-(b) Q2A1T6, (c)-(d) Q2A1T12, (e)-(f) Q8A1T18.

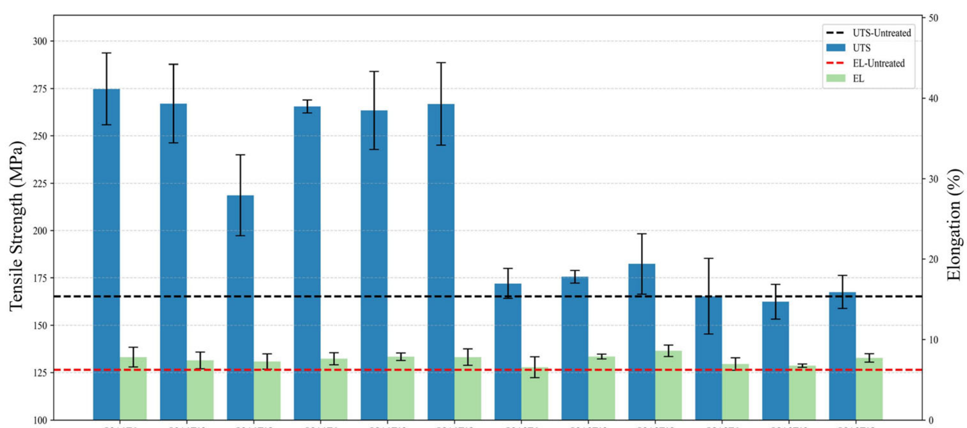

Figure 8. The tensile tests result for different HT and quenching temperature.

Another critical factor affecting the mechanical behavior of A380 aluminum alloy is the quenching temperature. The data suggests that quenching at 20°C results in higher tensile strengths compared to quenching at 80°C. For instance, the tensile strength for a sample heat treated for 6 hours and quenched at 20°C was 274.7 MPa, whereas quenching at 80°C resulted in a tensile strength of 265.5 MPa. Quenching at 20°C results in rapid cooling, which effectively "freezes" the microstructure, trapping precipitates in a fine, well-dispersed state. This finer distribution of precipitates contributes to the higher tensile strengths observed in these samples.[25] In contrast, quenching at 80°C slows the cooling rate, allowing for increased diffusion of solute atoms and precipitate coarsening. The larger precipitates formed at the higher quenching temperature weaken the material's mechanical properties, resulting in lower tensile strength.[26]

The change in HT temperature from 175°C to 275°C appears to have a significant impact on the tensile properties of the alloy. HT at 275°C, regardless of the quenching temperature, led to lower tensile strengths when compared to HT at 175°C. The samples quenched at 20°C and subjected to HT at 275°C for 6, 12, and 18 hours exhibited tensile strengths of 172, 175.5, and 182.2 MPa, respectively. Similarly, the samples quenched at 80°C and heat treated at 275°C displayed tensile strengths of 165.2, 162.4, and 167.5 MPa for the same respective durations. The decrease in tensile strength during HT at 275°C suggests that exposure to higher temperatures can have a detrimental impact on the mechanical properties of the A380 alloy. At 275°C, the precipitates in the A380 aluminum alloy may be growing in size and coarsening. Larger precipitates reduce the alloy's ability to resist deformation and dislocation movement, resulting in a decrease in tensile strength.[27] The lower tensile strengths observed at 275°C might make this temperature less favorable for specific applications where high mechanical strength is required.

Aluminum alloys like A380 often benefit from solid solution strengthening, where alloying elements are dissolved into the aluminum matrix, enhancing its strength. However, exposure to higher temperatures like 275°C can lead to the partial or complete dissolution of these alloying elements, reducing their strengthening effect.[9] This can result in a decrease in tensile strength. At 275°C, the alloy might undergo phase transformations that are unfavorable for its mechanical properties. Certain phases formed during HT can have a negative impact on the alloy's strength. For example, the transformation of a strengthening phase to a less effective phase at this temperature can contribute to the observed reduction in tensile strength.

When the ductility of the samples is evaluated, the percentage elongation results are highest in the NT samples ($\sim$8-10%), indicating the superior ductility of the samples in the as-cast condition. In all heat-treated groups, however, the percentage elongation decreases to approximately 2-3%, demonstrating a significant increase in brittleness following heat treatment. It is also observed that the aging durations tested (6-18 hours) do not have a meaningful effect on either the tensile strength or ductility, suggesting that these durations are sufficient for the precipitation mechanism to reach equilibrium.

The results have important implications for the practical use of A380 aluminum alloy in various industries. They suggest that a careful selection of quenching and HT conditions is necessary to modify the material's mechanical properties to specific requirements. The results can be used to optimize the HT process for A380 aluminum alloy, considering the trade-offs between tensile strength, ductility, and other desirable properties.

In Figure 9, representative stress–strain curves of A380 alloy samples applied to quenching at 80°C and different aging times at 175°C are presented. In all curves, the low amount of plastic deformation and sudden fracture points indicate that the fracture in the samples occurred in a brittle character. While the highest strength and ductility were obtained in 6-hour aging, a significant decrease in the mechanical performance of the material was observed in longer periods due to the coarsening of the precipitates.

SEM analysis was performed on the fractured surface of the two samples that had been subjected to tensile testing. From the samples heat treated at 175 °C and 275 °C degrees, one representative sample was selected from each. Images of the samples at 5kX and 3kX magnification are given in Figure 10. During examination of the fracture surface of the 175 °C sample, it is observed that it generally fractures brittle but partially ductile. A brittle fracture form was observed in the sample taken from the group of 275 °C.

Microhardness

Figure 11 presents the microhardness of the heat-treated and untreated samples. The untreated sample exhibited a hardness of 107.9 HV. This value is used to compare heat-treated samples. A heat-treated sample at 275°C has a lower hardness value than an untreated sample, whereas a heat-treated sample at 175°C has a higher hardness value. Increasing the aging temperature beyond its optimal level causes over-aging.[26] This can be observed from the hardness value at 275°C. As the aging temperature increases, the precipitate particles continue to coalesce and form larger precipitates, depending on the aging time. Large precipitates cause developing dislocations to be easier, which severely affects the mechanical properties of the aluminum alloys.

Hardness increased gradually in specimens heat treated at 175°C with an increase in HT time. A similar increase was not observed in samples at 275°C. The highest level of hardness was observed at 12 hours (87.7 HV) and 6 hours (95.6 HV) of HT times for samples heat treated at 275°C and quenched at 20°C and 80°C, respectively. Among all the samples, the highest hardness value 151.4 HV was found in the samples that were quenched at 20°C and heat treated at 175°C for 18 hours. This hardness value is approximately 40.3% higher than hardness of the untreated

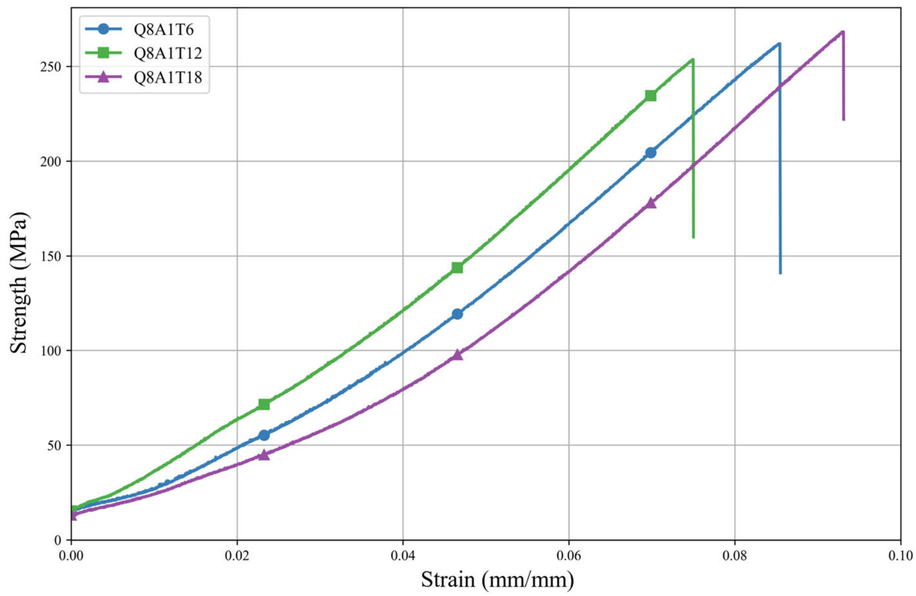

Figure 9. The stress–strain curves of samples quenched at 80°C and aged at 175°C for different durations.

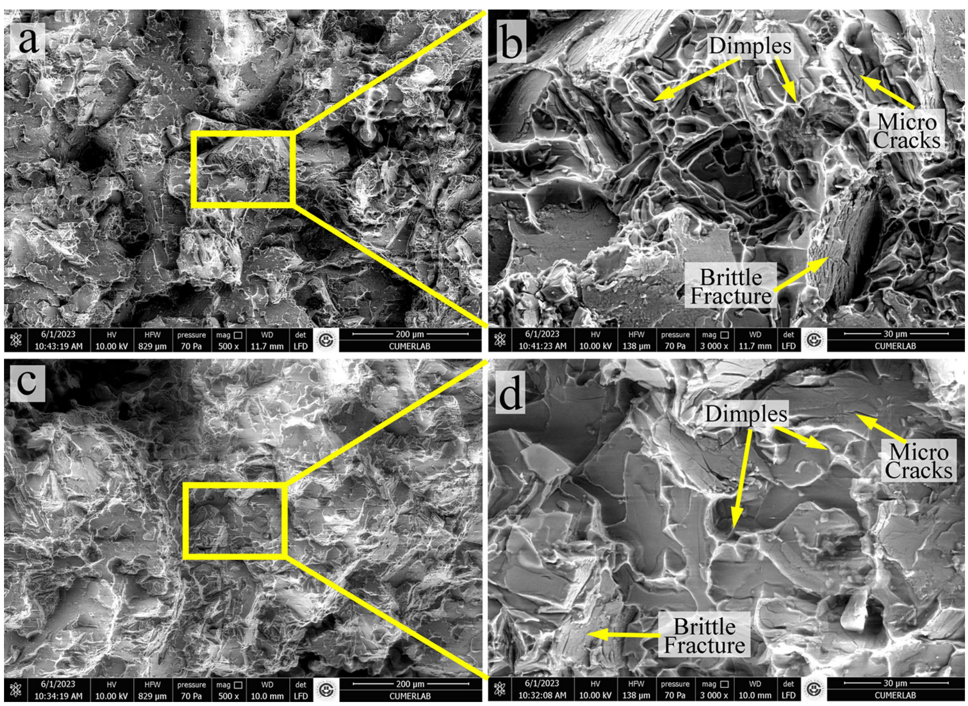

Figure 10. SEM images of fracture area, (a) aged at 175°C in 500X, (b) aged at 175°C in 3000X, (c) aged at 275°C in 500X, (d) aged at 275°C in 3000X.

sample. Similarly, the highest hardness value of 148.2 HV was obtained in the samples quenching at 80°C and heat treated at 175°C for 18 hours.

Wear

Wear tests were carried out with a Ø6 mm AISI 304 stainless steel ball under dry sliding conditions using a ball-on-disk wear test configuration to investigate the tribological behavior of the heat-treated and untreated samples.

Experimental Evaluation of Wear Behavior

The variation of the coefficient of friction (COF) recorded during the test is shown in Figure 12. All samples along the wear distance had a running-in period. Although the duration of this period varied between samples, it was observed that the running-in process was completed by approximately 15 meters in all cases. During the running-in period, the COFs of the samples increased due to the formation of adhesive contacts under high initial surface pressure and then partially decreased. After this stage, the COFs became stable as the real contact area increased. In the initial meters of wear tests, the small contact area leads to high surface pressure, forming adhesive bonds between surfaces. These adhesive bonds resist slipping, causing the friction coefficient to increase.[28] In the next period, the COF becomes stable as the contact area increases. Despite this stabilization, some fluctuations were still observed, attributed to material transfer between the contact surfaces.[29]

The average COFs and wear rates of the samples are given in Figure 13. The highest wear rate was obtained in the untreated sample. In other samples, it has been observed that quenching and artificial aging processes increase wear resistance.

When comparing samples quenched at 20°C, the wear rates of the sample group aged at 175°C were higher than those aged at 275°C. The hardness of the samples quenched at 20°C and aged at 175°C is higher than the samples

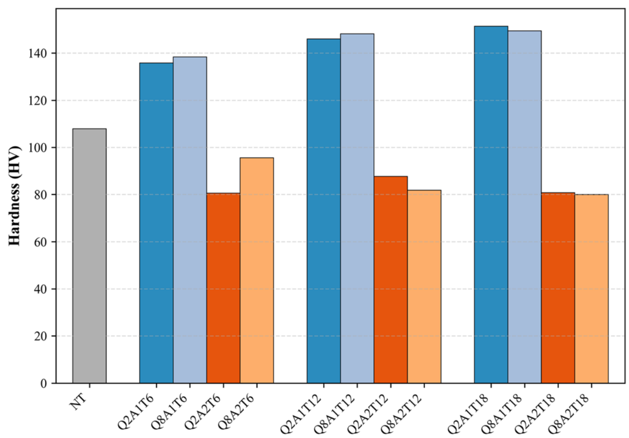

Figure 11. Microhardness of the samples.

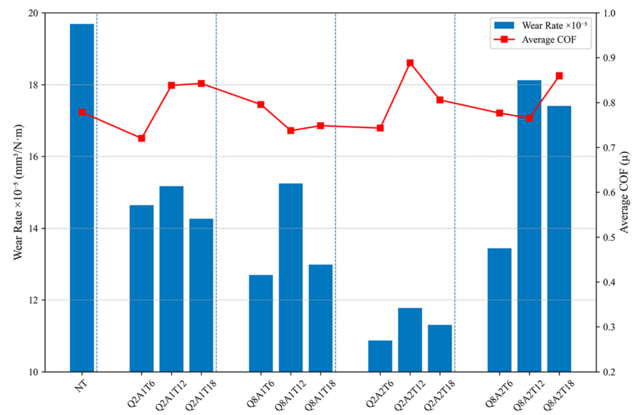

Figure 13. Wear rate and average COF of the samples.

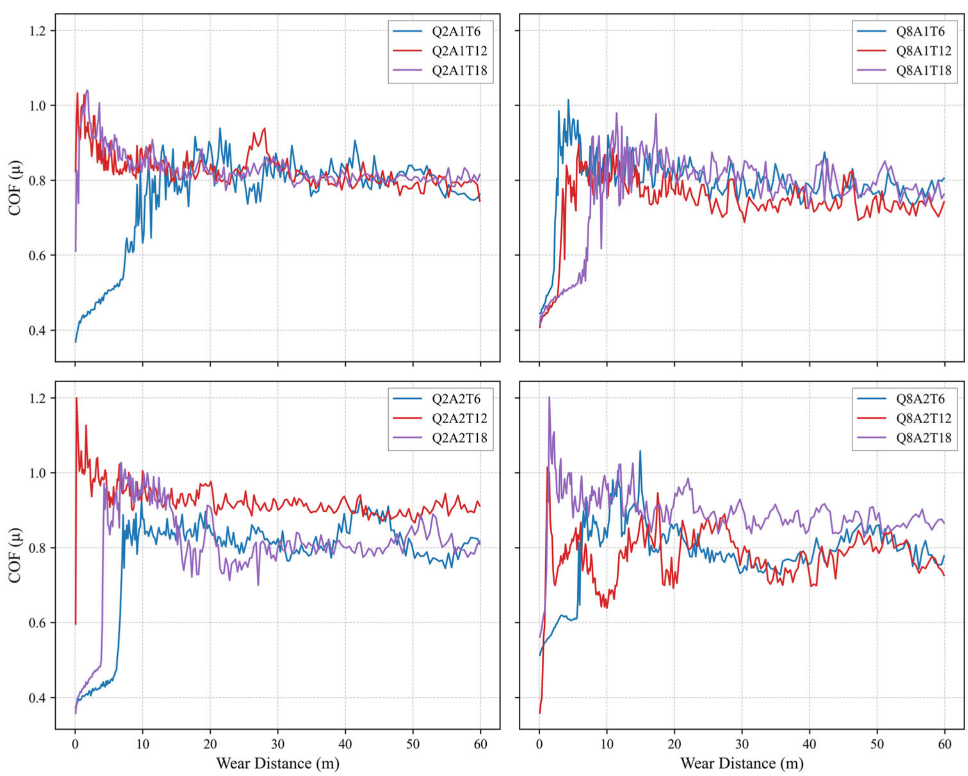

Figure 12. Variation of the COF with wear distance.

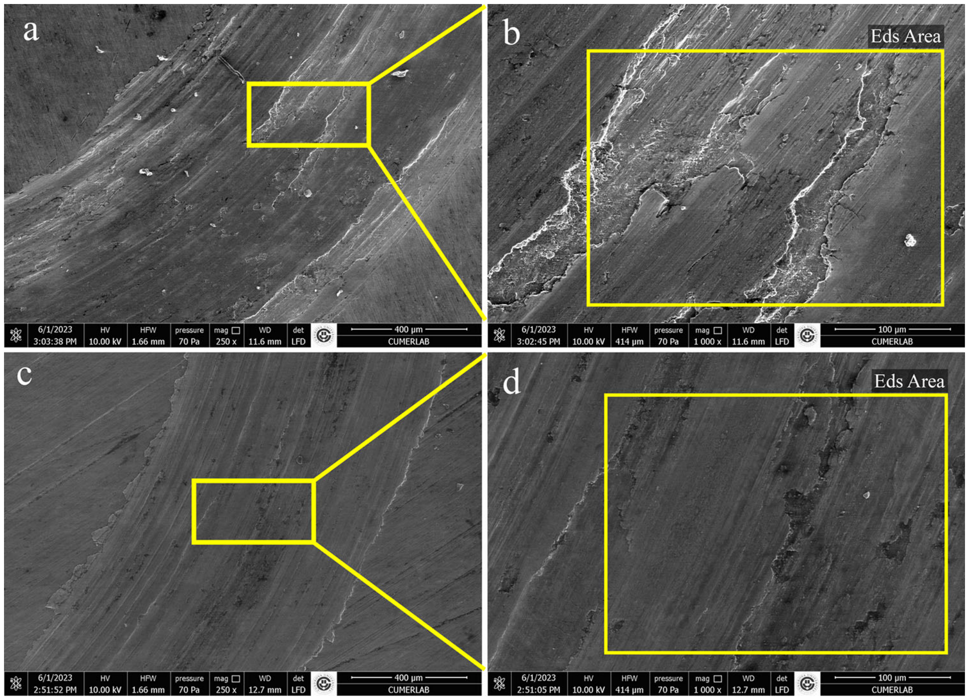

Figure 14. SEM images of worn area, (a), (b) Q8A1T12 (c), (d) Q2A2T12.

quenched at 20°C and aged at 275°C. During the wear test, hard particles fractured from the surface of the samples due to contact with the counter body. The fractured particles acted as a third object and increased the abrasive wear rate on the sample surface. Samples quenched at 20°C and aged at 275°C yielded the best wear resistance among the experimental groups. Some of the relatively softer fractured particles break off from the surface during the wear tests and re-adhered to the sample surface, contributing to adhesive wear. Due to the influence of this adhesive wear, the wear rate in these samples did not increase significantly. Furthermore, the EDS results provided in Table 3 indicate that the oxygen content on the wear surface of the samples quenched at 20°C and aged at 175°C is higher. This oxygen formed an oxide layer on the surface and reduced the contact surface area, preventing the increase in wear rate. Oxide layers decreases real contact area between the two metal contacts.[30]

High hardness values were obtained for the samples group quenched at 80°C and aged at 175°C as like the samples quenched at 20°C and aged at 175°C. The hard particles that fractured during the wear tests acted as a third object which caused an increase in the wear rate. Compared to the other HT samples, the highest wear rate was obtained in the samples 12 and 18 hours aged at 275°C and quenched at 80°C. As explained in the hardness section, large precipitates formed in samples quenched at 80°C aged at 275°C. Due to the effect of large precipitates, the non-hard surface was fragmented by the counter body and therefore, the wear rate increased. In these samples, adhesive wear has not been observed as much as in the other sample group heat treated at 275°C (quenched at 20°C), which caused the wear rate to increase. In each group, the wear rates of the samples at 12-hour aging time are higher than those at 6 and 18 hours. The increase in the wear rate at 12 hours compared to 6 hours was due to the effect of hard particles breaking off the sample surface. The relatively softer particles that broke off from the surface in 18 hours compared to 12 hours caused adhesive wear, causing the wear rate to decrease slightly. In comparison with the untreated sample, samples quenched at 20°C and aged at 275°C for 6 hours performed the best in wear resistance with an 81.2% improvement.

Table 3. EDS Analysis of the Samples

Composition (wt%)						
EDS area	Al	Si	Cu	Fe	Cr	O
Figure 14b	77.13	7.08	2.15	0.54	0.89	12.22
Figure 14d	63.01	5.59	1.65	0.92	1.29	27.54

Figure 14 shows representative SEM images of the worn surfaces of Q8A1T12, and Q2A2T12 samples at 250X and 1000X magnifications. EDS analyses obtained at SEM 1000X magnification are given in Table 3.

The worn surfaces of heat-treated samples showed adhesion and delamination layers. During the test, the pieces that break off from the wear surface either move away or get stuck between the ball and the surface. The particles stuck in between stick to the surface again under the force's effect, creating adhesion wear. As the test progresses, the sticky particles break off, forming a partial delamination layer.

Data-Driven Prediction of Specific Wear Behavior Using Supervised Learning Models

In addition to the conventional mechanical interpretation of the wear behavior, data-driven predictive modeling approaches were also employed to evaluate the consistency and explanatory power of the experimental results. Given the complex and nonlinear nature of wear phenomena, particularly in heat-treated aluminum alloys, machine learning-based regression models offer a promising alternative for estimating specific wear rates. In this context, several supervised learning algorithms, including both traditional ensemble models and neural network-based architectures, were implemented and compared.

The performance of DNN and MLPR models used in predicting the specific wear rate values of heat-treated aluminum A380 alloy samples was evaluated through loss-epoch graphs. The graph presented in Figure 15 shows the learning processes of both models around 300 epochs.

The given epoch loss graph compares the learning behaviors of MLPR and DNN models during the training process. The MLPR model starts with a very high error value at the beginning and exhibits a rapid decrease during the first 50 epochs, sharply decreasing the learning curve. However, after the 50th epoch, the improvement slows down and the model plateaus at approximately 3-5 MSE levels and reaches saturation in learning. In contrast, the DNN model started training with a lower initial error and was much more stable and stable, with low oscillations, fixed at around 2 MSE. This shows that the DNN model both has a more stable learning process and results in higher accuracy in general. In particular, the smooth and balanced loss decrease in the DNN curve shows that the model works more efficiently in terms of regularization and optimization. This graph reveals that DNN is better than MLPR not only in terms of accuracy but also in terms of training process stability.

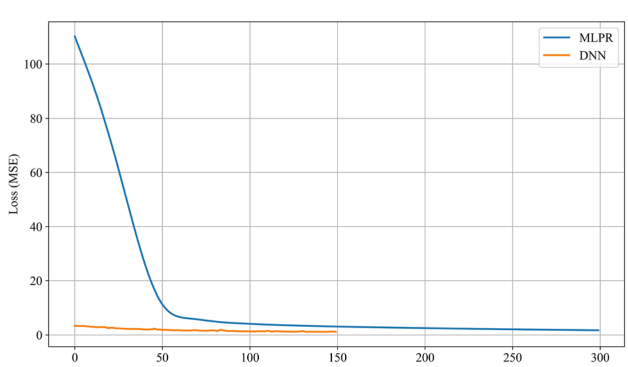

Figure 15. Loss epoch performance of the MLPR and DNN models.

The distribution graphs of the obtained actual and predicted values given in Figure 16 provide important information in terms of visualizing the predicted performances of the models.

According to the scatter plots showing prediction–measurement comparisons of the training data, RF and DNN models showed high fit thanks to the positioning of the actual vs. predicted points close to the perfect fit line. These models successfully learned the general trend in data distribution and performed the regression performance with high accuracy. On the other hand, increasing deviations were observed at high values in DT, GB, and XGB models; this situation suggests that these models cannot provide sufficient generalization at the upper limits. Especially the MLPR model showed significant deviations in terms of distribution and showed low accuracy even on the training data. This result indicates that the learning capacity of the model is insufficient for the current problem.

Table 4 presents the specific wear rate values corresponding to different heat treatment conditions (quenching temperature, aging temperature, and time), along with their predictions and the calculated absolute percent error (APE) for each data point. The table display quantifies not only the overall model performance but also how prediction accuracy varies under specific process parameters.

Considering the experimental results, it appears that the model error rates generally remain low until a steady improvement in wear resistance is achieved. For more regular variations in specific wear rates, all models generally achieved low APE. This is due to the more predictable nature of the material's tribological behavior under certain parameter combinations, and to the models' ability to better understand the data distribution under these conditions. For slight fluctuating in specific wear rates, such as those observed in the Q2A1T12 and Q2A2T12 samples, tree-based prediction models demonstrated strong generalization capability, attaining APE of 1–2%, whereas neural network-based models underperformed relative to the others, exhibiting comparatively higher APE in the range of 7–10%. Furthermore, tree-based models show inherent limitations in capturing nonlinear fluctuations in the specific wear rate, particularly the pronounced decrease that follows sharp increases at the 6th and 12th hours, as observed in case Q8A1T18. In contrast, neural network-based models exhibit a superior capacity to accurately represent these dynamic variations. APE metric can be considered a critical complementary metric not only for model comparison but also for revealing the impact of heat treatment parameters on the wear mechanism and its

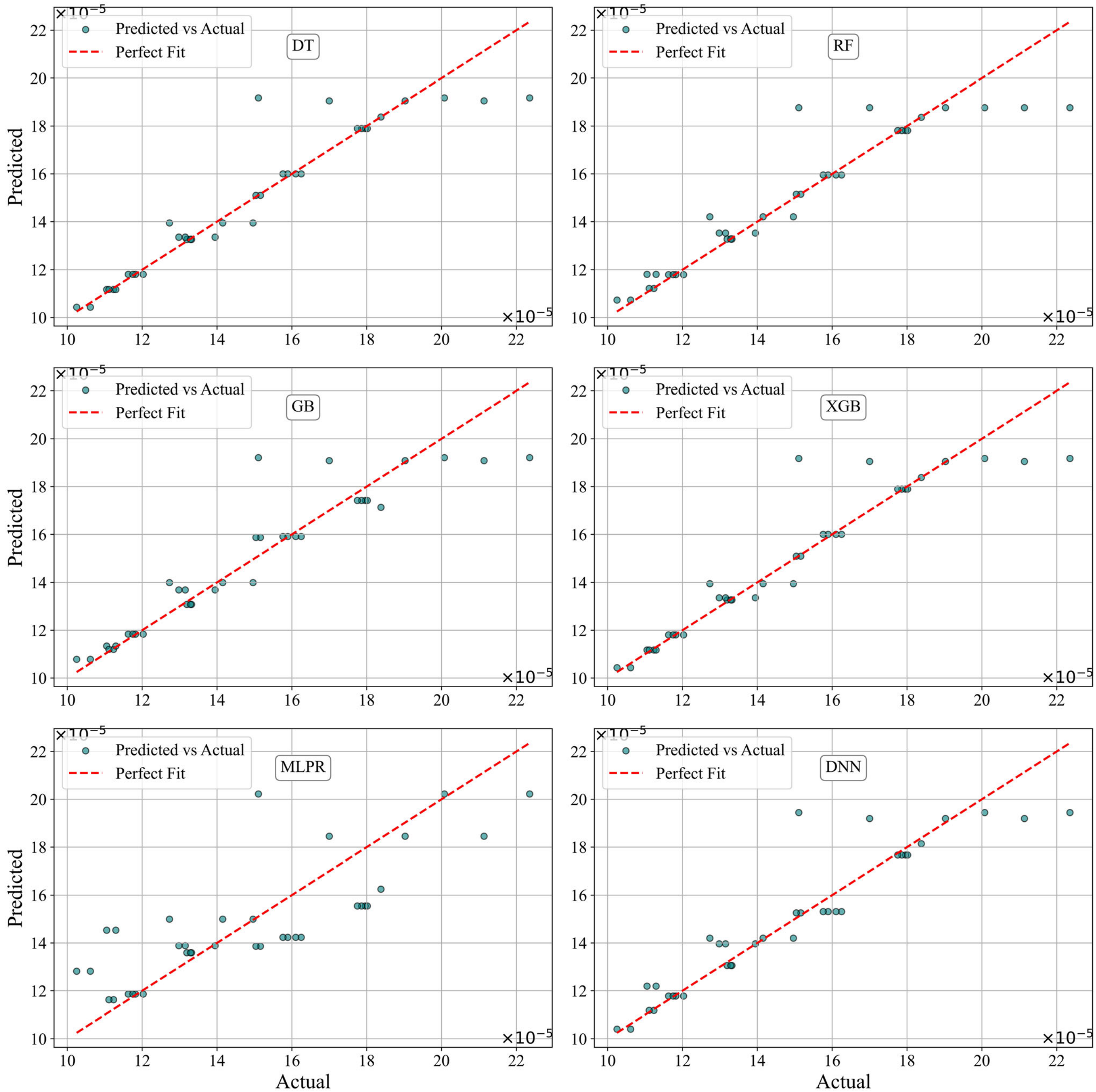

Figure 16. Performance of the predictive models on the train samples.

impact on predictive accuracy. Figure 17 shows the mean absolute percentage error (MAPE) of the predictive models.

The MAPE results in Figure 17 shows that XGB and DT stand out in terms of predictive performance, showing the lowest error rates, while the RF model, with a similarly low error, demonstrates the tree-based models' success in generalizing tribological behavior. The GB model produced a relatively higher error but captured the general trends. In contrast, the MLPR, and especially, the DNN models exhibited poorer performance, with error rates increasing significantly under extreme aging conditions and under deterioration of mechanical homogeneity due to precipitation growth. These results indicate that tree-based models provide more reliable prediction accuracy, while neural network-based models have higher error rates in response to fluctuations in tribological behavior. Consequently, the effect of heat treatment parameters on the wear mechanism directly determines model accuracy.

The bar charts in Figure 18 evaluate the prediction performances of the models in the test and validation sets in terms of both MSE and R^2 score.

Table 4. APE for Each Predictive Model (Actual, Pred. x $10^{-5} mm^3/N.m$)

		DT		RF		GB		XGB		MLPR		DNN	
HT Param.(input)	Actual	Pred.	APE	Pred.	APE	Pred.	APE	Pred.	APE	Pred.	APE	Pred.	APE
Q8A2T6	12.95	13.94	7.70	14.01	8.22	13.99	8.05	13.94	7.70	14.99	15.78	15.28	18.03
Q8A1T18	16.17	11.17	30.93	11.67	27.84	11.34	29.89	11.17	30.92	14.53	10.16	14.16	12.44
Q2A1T18	13.46	13.26	1.43	13.26	1.44	13.07	2.82	13.26	1.43	13.59	0.98	13.93	3.54
Q8A2T12	18.07	18.38	1.69	18.36	1.62	17.12	5.21	18.37	1.69	16.24	10.10	16.71	7.49
Q2A1T12	14.96	15.1	0.93	15.03	0.48	15.87	6.10	15.09	0.93	13.86	7.33	13.98	6.48
NT	21.82	19.17	12.12	19.05	12.67	19.20	11.97	19.17	12.12	20.22	7.33	21.39	1.93
Q2A2T6	10.39	10.43	0.33	10.82	4.10	10.78	3.72	10.43	0.35	12.81	23.25	13.53	30.12
Q8A1T6	13.22	13.35	0.97	13.52	2.20	13.68	3.47	13.35	0.97	13.88	4.95	13.92	5.22
Q2A2T6	10.55	10.43	1.19	10.82	2.52	10.78	2.14	10.43	1.16	12.81	21.37	13.53	28.14
Q2A2T12	11.19	11.17	0.15	11.39	1.83	11.20	0.10	11.17	0.14	11.62	3.88	12.23	9.36

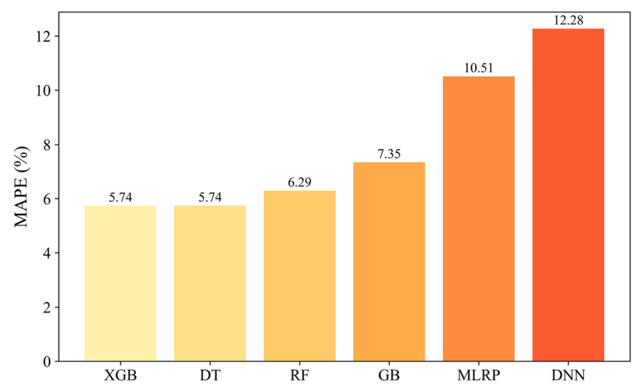

Figure 17. MAPE of the predictive models.

According to the scatter plots on the train set, the RF and DNN models, which provided the highest fit, successfully demonstrated their generalization abilities by maintaining their consistent performance in the test and validation sets. While the RF model draws attention with both low MSE and high R^2 values; the DNN model stands out with the lowest error (MSE $\approx$ 1.7) and the highest explanation ratio (R^2 $\approx$ 0.85) especially in the test set. While it is seen that these two models draw prediction curves quite close to the real data in the test line plots, it is also observed that the consistency of RF and the general trend are followed successfully in the validation line plots despite the slight deviations of DNN. In the other models, the increasing error and decreasing R^2 scores in the validation set indicate generalization problems and remain weak compared to the train-test fit. As a result, when both quantitative error metrics and visual analyzes are taken into account, the RF model exhibits high reliability and stability, while the DNN model offers a significant alternative especially in terms of accuracy.

Validation part assesses the real generalization ability of the models on new examples that they have never seen. At this stage, the RF model provided the most stable and reliable results by maintaining the prediction values with minimum deviation. Although the DNN model showed slightly increased deviations in the validation set compared to the test set, it followed the general direction and showed an acceptable generalization success. Other models, especially XGB and MLPR, performed worse in the validation

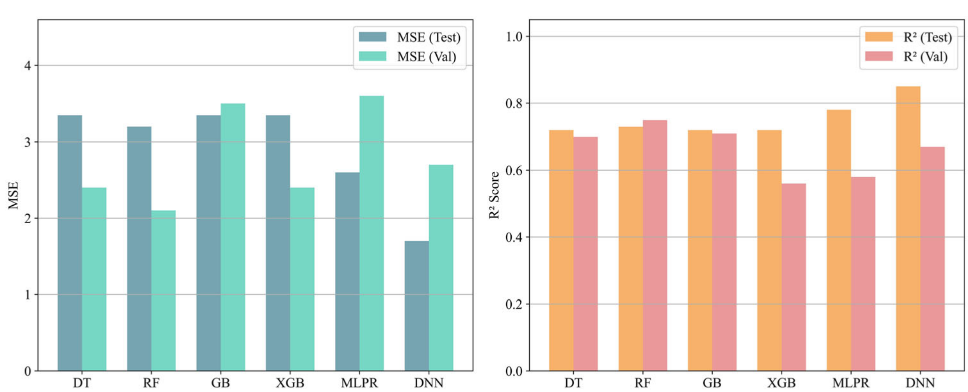

Figure 18. Performance of the models on test and validation set by MSE and R^2 score.

Table 5. Results of the Cross-Validated Permutation Importance Analysis

Feature	ΔMSE	CI bounds	Top rank frequency
Aging	8.59	6.53-10.65	%60
Quenching	7.86	5.35-10.37	%40
Time	4.14	3.63-4.64	%10

set compared to the test set. In terms of validation accuracy, the GB and DT models could not maintain their performance compared to the test set and remained weak in generalization ability.

Table 5 presents the cross-validated permutation importance results of the Random Forest model, which quantify the relative contribution of each heat-treatment parameter to the prediction of the specific wear rate. The Mean "ΔMSE" indicates the average increase in mean squared error when the corresponding feature is permuted, while the 95% confidence interval (CI) bounds describe the statistical reliability of that increase. The "Top-rank frequency" represents how consistently each variable appears as the most influential feature across the cross-validation folds, thus serving as an indicator of model stability.

Among the examined parameters, aging temperature emerged as the most dominant feature, exhibiting the highest mean ΔMSE value (8.59) and a narrow confidence interval (6.53–10.65). It ranked first in 60% of the validation folds, demonstrating a strong and stable impact on the model's predictive performance. This finding confirms that the aging temperature is the primary factor governing the wear behavior of A380 alloy by controlling precipitation kinetics and the microstructural refinement process. In particular, higher aging temperatures promote the coarsening of precipitates and reduce surface hardness, thereby increasing the specific wear rate. The findings of the present study are fully consistent with the literature, where several independent investigations have also reported that aging temperature is the most influential parameter governing the mechanical and tribological behavior of heat-treated aluminum alloys.[31,32] .The quenching temperature, ranked second with a mean ΔMSE of 7.86, showed moderate variability and an indirect influence on wear resistance through microstructural homogeneity, whereas the aging time exhibited the lowest but consistent effect, indicating a secondary contribution compared to temperature-related parameters.

Conclusions

In this study, the effects of T6 heat treatment parameters of A380 aluminum alloy on mechanical properties and wear behavior were investigated comprehensively by experimental and machine learning-based analyses. The findings revealed that room temperature quenching (20°C) and aging at 175°C reached the highest values in terms of tensile strength and hardness but increasing this period beyond 18 hours caused excessive aging, leading to a decrease in mechanical performance. On the other hand, it was determined that high aging temperatures such as 275°C had negative effects especially on microhardness and tensile strength, and this situation was associated with a microstructure that could not prevent dislocation movement due to the formation of large precipitates. Wear experiments showed that the samples aged at 275°C and cooled at 20°C exhibited the highest performance in wear resistance. This improvement was associated with the reduction of the oxide layer formed on the surface and adhesive wear.

Another important contribution of the study is the analysis of experimental data with machine learning models. Among the regression models developed, Random Forest and Deep Neural Network models achieved the highest accuracy rates, and the Deep Neural Network model stood out with low error and high explanatory power ($R^2 \approx 0.85$), especially in the test data. These models have high potential in predicting the wear behavior of the A380 alloy and can form the basis of data-driven design processes that will provide efficiency in industrial applications.

As a result, for the A380 alloy, quenching at 20°C and aging at 175°C for 6 to 12 hours are recommended in order to obtain optimum mechanical properties. In terms of wear resistance, aging at 275°C for 6 hours provides the most successful performance when considered together with appropriate cooling conditions. In further studies, it is recommended to examine the microstructure–property relationships in more detail together with the characterization of different precipitation hardening mechanisms. In addition, the developed machine learning models can be fed with larger data sets to increase their generalization success and thus be integrated into real-time production processes.

REFERENCES

1. I. Polmear, D. StJohn, J.-F. Nie, and M. Qian, *Light alloys: metallurgy of the light metals*. Butterworth-Heinemann, (2017)
2. G.K. Sigworth, F. DeHart, Recent developments in the high strength aluminum-copper casting alloy A206. AFS Trans. **111**, 341–354 (2003)
3. M. Çolak, İ Arslan, Investigation of the effect of the addition of grain refiner and modifier addition on wear properties in sand and permanent mould casting of A357 and A380 aluminium alloys. Int. J. Cast Met.

Res. (2022). https://doi.org/10.1080/13640461.2022.2069912
4. M. Çolak, D. Dispinar, The influence of metallostatic pressure, grain refiner, and modification on the critical solid fraction (CSF) of cast A380 alloy. J. Engg. Res. **9**(4B), 269–280 (2021). https://doi.org/10.36909/jer.8328
5. E. Uslu, A. Tiğli, M. Çolak, The effect of cooling plate, mechanical vibration, and grain refinement on the microstructure and hardness of A380 produced by sand mold. Int. J. Cast Met. Res. (2023). https://doi.org/10.1080/13640461.2023.2299912
6. S. Gencalp, N. Saklakoglu, Semisolid microstructure evolution during cooling slope casting under vibration of A380 aluminum alloy. Mater. Manuf. Process. **25**(9), 943–947 (2010). https://doi.org/10.1080/10426911003636944
7. S. Seifeddine and I.L. Svensson, The influence of Fe and Mn content and cooling rate on the microstructure and mechanical properties of A380-die casting alloys. Metallurgical Science and Tecnology. **27** (1), (2009).
8. K.N. Obiekea, S.Y. Aku, D.S. Yawas, Effects of pressure on the mechanical properties and microstructure of die cast aluminum A380 alloy. J. Miner. Mater. Charact. Eng. **2**(03), 248 (2014)
9. R. Gecu, S. Acar, A. Kisasoz, K. Altug Guler, A. Karaaslan, Influence of T6 heat treatment on A356 and A380 aluminium alloys manufactured by thixoforging combined with low superheat casting. Trans. Nonferrous Met. Soc. China **28**(3), 385–392 (2018). https://doi.org/10.1016/s1003-6326(18)64672-2
10. M. Zhang, Y. Tian, X. Zheng, Y. Zhang, L. Chen, J. Wang, Research progress on multi-component alloying and heat treatment of high strength and toughness Al–Si–Cu–Mg cast aluminum alloys. Materials **16**(3), 1065 (2023)
11. S. Khisheh, K. Khalili, M. Azadi, V.Z. Hendouabadi, Influences of roughness and heat treatment on high-cycle bending fatigue properties of A380 aluminum alloy under stress-controlled cyclic loading. Mater. Chem. Phys. **264**, 124475 (2021)
12. Z. Yuan, Z. Guo, S. Xiong, Effect of as-cast microstructure heterogeneity on aging behavior of a high-pressure die-cast A380 alloy. Mater Charact **135**, 278–286 (2018)
13. H. Yang, S. Ji, W. Yang, Y. Wang, Z. Fan, Effect of Mg level on the microstructure and mechanical properties of die-cast Al–Si–Cu alloys. Mater. Sci. Eng. A **642**, 340–350 (2015)
14. S. Gajević, S. Miladinović, O. Güler, S. Özkaya, B. Stojanović, Optimization of dry sliding wear in hot-pressed Al/B4C metal matrix composites using taguchi method and ANN. Materials. **17**(16), 4056 (2024)
15. P. Muthu, Multi objective optimization of wear behaviour of Aluminum MMCs using Grey-Taguchi method. Manuf. Rev. **7**, 16 (2020). https://doi.org/10.1051/mfreview/2020013. (**[Online]. Available:**)
16. E. Sjölander, S. Seifeddine, The heat treatment of Al–Si–Cu–Mg casting alloys. J. Mater. Process. Technol. **210**(10), 1249–1259 (2010)
17. E. Ogris, A. Wahlen, H. Lüchinger, P. Uggowitzer, On the silicon spheroidization in Al–Si alloys. J. Light. Met. **2**(4), 263–269 (2002)
18. J. Wang, J. Zhu, Y. Liu, H. Peng, X. Su, Effect of spheroidization of eutectic Si on mechanical properties of eutectic Al–Si alloys. J. Mater. Res. **33**(12), 1773–1781 (2018)
19. H. Borkar, S. Seifeddine, A.E. Jarfors, Microstructure, texture and mechanical properties of Al alloy A380 prepared by directional solidification method. Solid State Phenom. **287**, 18–23 (2019)
20. L. Ceschini, A. Morri, S. Toschi, S. Johansson, S. Seifeddine, Microstructural and mechanical properties characterization of heat treated and overaged cast A354 alloy with various SDAS at room and elevated temperature. Mater. Sci. Eng. A **648**, 340–349 (2015)
21. S.G. Irizalp, N. Saklakoglu, Effect of Fe-rich intermetallics on the microstructure and mechanical properties of thixoformed A380 aluminum alloy. Eng. Sci. Technol. Int. J. **17**(2), 58–62 (2014). https://doi.org/10.1016/j.jestch.2014.03.006
22. Q. Lan, X. Wang, J. Sun, Z. Chang, Q. Deng, Q. Sun, Z. Liu, L. Yuan, J. Wang, Y. Wu, Artificial neural network approach for mechanical properties prediction of as-cast A380 aluminum alloy. Mater. Today Commun. **31**, 103301 (2022). https://doi.org/10.1016/j.mtcomm.2022.103301
23. F. Jiang, J. Huang, Y. Jiang, C. Xu, Effects of quenching rate and over-aging on microstructures, mechanical properties and corrosion resistance of an Al–Zn–Mg (7046A) alloy. J. Alloys Compd. **854**, 157272 (2021). https://doi.org/10.1016/j.jallcom.2020.157272
24. M. Usta, M.E. Glicksman, R.N. Wright, The effect of heat treatment on Mg2Si coarsening in aluminum 6105 alloy. Metall. Mater. Trans. A **35**(2), 435–438 (2004). https://doi.org/10.1007/s11661-004-0354-7
25. W. Khalifa, S. El-Hadad, Ultrasonication effects on the microstructure characteristics of the A380 die cast alloy. Int. J. Metalcast. **13**(4), 865–879 (2019). https://doi.org/10.1007/s40962-018-00296-8
26. C.F. Tan, S.M. Radzai, Effect of hardness test on precipitation hardening aluminium alloy 6061–T6. Chiang Mai J. Sci. **36**(3), 276–286 (2009)
27. W. Wen, Y. Zhao, J.G. Morris, The effect of Mg precipitation on the mechanical properties of 5xxx aluminum alloys. Mater. Sci. Eng. A **392**(1), 136–144 (2005). https://doi.org/10.1016/j.msea.2004.09.059
28. M. Beder, Y. Alemdag, Influence of Mg addition and T6 heat treatment on microstructure, mechanical and tribological properties of Al–12Si–3Cu based alloy. Trans. Nonferrous Met. Soc. China **31**(8), 2208–2219

(2021). https://doi.org/10.1016/S1003-6326(21)65649-2

29. Y. Alemdag, M. Beder, Effects of Mn content on microstructure, mechanical and dry sliding wear properties of eutectic Al–Si–Cu alloy. Met. Mater. Int. **26**(12), 1811–1819 (2020). https://doi.org/10.1007/s12540-019-00572-0
30. K. Kılıçay, E. Kaya, Improvement of microstructural and tribological properties of APS carbide coatings via PTA surface melting. Transactions of the IMF. **98**(3), 129–137 (2020). https://doi.org/10.1080/00202967.2020.1753408
31. R. Jojith, N. Radhika, M. Govindaraju, Reciprocating wear behavioural analysis of heat-treated aluminium ZrO2/Al7Si0.3Mg functionally graded composite through Taguchi's optimization method. SILICON **14**(17), 11337–11354 (2022). https://doi.org/10.1007/s12633-022-01862-w
32. A. Mehmood, K. Akhtar, S. Noor, M.Z. Zahir, B. Ullah, R. Khan, B. Salah, S. Sajid Ullah, Experimental study to optimize cold working, aging temperature, and time on the properties of AA6061 tubes: analysis using design of experiment. Front. Mater. **10**, 1199099 (2023)